Editors' Suggestion

Real-Time Charge Initialization of Diamond Nitrogen-Vacancy Centers for Enhanced Spin Readout

David A. Hopper,[1,2] Joseph D. Lauigan,[1,†] Tzu-Yung Huang,[1] and Lee C. Bassett[1,*]

[1] *Quantum Engineering Laboratory, Department of Electrical and Systems Engineering, University of Pennsylvania, 200 South 33rd Street, Philadelphia, Pennsylvania 19104, USA*

[2] *Department of Physics and Astronomy, University of Pennsylvania, 209 South 33rd Street, Philadelphia, Pennsylvania 19104, USA*

(Received 19 July 2019; revised manuscript received 27 November 2019; accepted 23 December 2019; published 7 February 2020)

A common impediment to qubit performance is imperfect state initialization. In the case of the diamond nitrogen-vacancy (N-V) center, the initialization fidelity is limited by fluctuations in the defect's charge state during optical pumping. Here we use real-time control to deterministically initialize the N-V center's charge state at room temperature. We demonstrate a maximum charge initialization fidelity of $(99.4 \pm 0.1)\%$ and present a quantitative model of the initialization process that allows system-level optimization of the spin-readout signal-to-noise ratio. Even when the overhead associated with the initialization sequence is accounted for, increasing the charge initialization fidelity from the steady-state value of 75% to nearly 100% allows a factor-of-2 speedup in experiments while maintaining the same signal-to-noise-ratio. In combination with high-fidelity readout based on spin-to-charge conversion, real-time initialization enables a factor-of-20 speedup over traditional methods, resulting in an estimated ac magnetic sensitivity of 1.3 $\mathrm{nT/Hz^{1/2}}$ for our single-N-V-center spin. The real-time control method is immediately beneficial for quantum-sensing applications with N-V centers as well as for probing charge-dependent physics, and it will facilitate protocols for quantum feedback control over multiqubit systems.

DOI: 10.1103/PhysRevApplied.13.024016

I. INTRODUCTION

The accelerating pace of quantum technology is evident in the advancement of quantum sensors [1] and the emergence of quantum networks [2]. Critical to these developments have been solid-state spin qubits based on semiconductor defects, due to their optical interface [3], compatibility with integrated technologies [4], and wide selection of host materials [5]. The most-well-known example is the nitrogen-vacancy (N-V) center in diamond [6,7], which has enabled pivotal advances in quantum sensing [8–14] and quantum-information processing [15–17].

One limitation to the performance of N-V-center qubits is imperfect initialization into the oft-desired negative charge state (N-V^-). Optical pumping with 532-nm light produces a steady-state statistical charge distribution; typically the probability to prepare the N-V^- state is around 75% [18,19], although it can be much lower for defects close to surfaces [20]. This probabilistic steady-state initialization (SSI) hampers spin readout by decreasing contrast and increasing readout noise [7], and it limits the fidelity of quantum gate operations of coupled spin systems using the N-V center as an ancilla [18,21]. Existing techniques to increase the charge initialization fidelity include doping electrically [22] or chemically [23], and multicolor optical pumping [24]. In addition, some experiments use postselection to filter out the noise [20,24–28]. These techniques either impose strict constraints on materials and device design or require elongated experimental runtime. At cryogenic temperatures, deterministic initialization protocols based on real-time feedback have been essential for entanglement generation and quantum error correction using N-V centers due to their long measurement times [16,29,30]; however, these techniques have not been adapted for quantum-sensing applications where the duration of each measurement cycle drastically affects the overall sensitivity.

Here we use real-time feedback to control a N-V center's charge-state initialization fidelity at room temperature, and we demonstrate increased spin readout efficiency and improved sensitivity. A model for the stochastic initialization procedure allows the selection of near-unity initialization fidelity into either charge state, or an arbitrary

*lbassett@seas.upenn.edu

†Present address: Quanergy Systems, 482 Mercury Drive, Sunnyvale, California 94085, USA.

intermediate charge distribution. We measure the influence of charge fidelity on the spin-readout signal-to-noise ratio (SNR) for two readout techniques, traditional photoluminescence (PL) and spin-to-charge conversion (SCC). Our comprehensive model allows the optimization of initialization and readout parameters for quantum control experiments of arbitrary durations. The real-time-initialization (RTI) protocol increases the spin-readout efficiency and reduces the time required for experiments; in combination with SCC readout, we demonstrate a factor-of-20 speedup as compared with traditional methods.

II. EXPERIMENTAL METHODS

A schematic of the experiment is shown in Fig. 1(a). The traditional portion of the setup consists of the lasers, microwave sources, diamond device, and photon-counting electronics. The sample is an electronic grade, type-IIa, synthetic diamond (Element Six) that has been irradiated with 2-MeV electrons (10^{14} cm^{-2}) and annealed at 800 °C for 1 h in forming gas. A solid immersion lens aligned to a single N-V center is fabricated by focused-ion-beam milling to increase the photon collection efficiency [24], resulting in a saturated count rate of 300 000 counts/s under 532-nm excitation [31]. Imaging and optical control are performed with a homebuilt room-temperature scanning confocal microscope with three excitation sources. A continuous-wave 532-nm laser (Gem 532, Laser Quantum), referred to as "green," is gated by an acousto-optic modulator (AOM) in a double-pass configuration; it is used for optical pumping and traditional PL readout. An amplitude-modulated 635-nm laser diode (MLD 06-01 638, Cobolt), referred to as "red," is used for charge readout and SCC. A continuous-wave 592-nm laser (VFL-592, MPB Communications Inc.), referred to as "orange," is gated with an AOM and is used for SCC. A 115-G magnetic field is aligned along the N-V axis to distinguish the $m_s = \pm 1$ states. A lithographically defined loop-antenna surrounding the solid immersion lens is driven by an amplified (ZHL-16W-43-S+, Mini-Circuits), amplitude-modulated (ZASWA-2-50DR, Mini-Circuits), continuous-wave signal generator (SG384, Stanford Research Systems), which allows ground-state spin control.

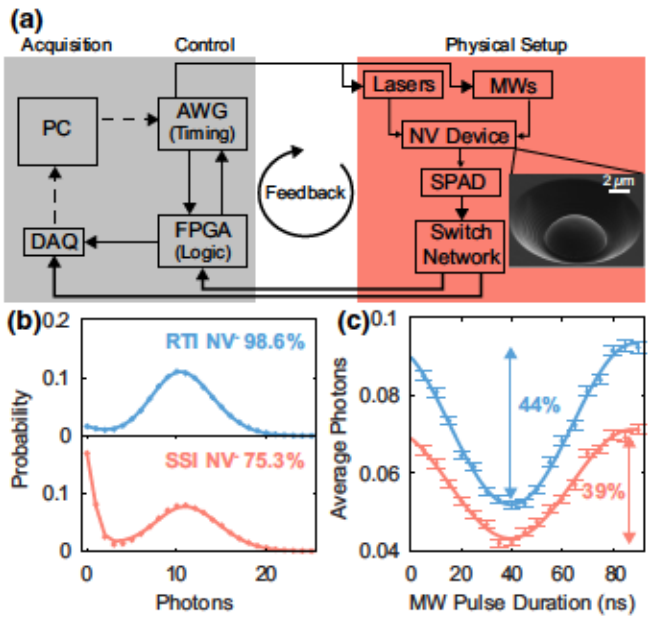

FIG. 1. Real-time charge initialization. (a) System overview for implementing real-time feedback on a N-V center's charge state. The inset shows a scanning electron micrograph of a solid immersion lens fabricated around a single N-V center. (b) Charge-readout distributions demonstrating the difference in charge-state initialization fidelity for the RTI (top panel) and SSI (bottom panel) protocols. (c) Rabi nutations of a single N-V center following RTI (top, blue curve and data points) and SSI (bottom, salmon curve and data points) demonstrating the increased signal and spin contrast (signified by the arrows). The curves are fits to the data using a sinusoidal oscillation. DAQ, data acquisition; MW, microwave; SPAD, single-photon avalanche diode.

The N-V center's charge state is determined to high accuracy by use of a wavelength that excites the N-V^- charge state (below the 637 nm zero-phonon line) but not the N-V^0 charge state (above the 575 nm zero-phonon line) [25]. Example histograms of photon counts arising from 75 000 charge readouts are shown in Fig. 1(b) for both the steady-state N-V^- population of $(75.3 \pm 0.4)\%$ and a higher-fidelity initial population of $(98.6 \pm 0.2)\%$. These populations are determined by fitting to a statistical model describing the observed photon number histogram [28]. The SSI value of approximately 75% agrees with previous measurements [19]. The benefit of this increased initialization fidelity can be seen in the ground-state Rabi nutations in Fig. 1(c), where the higher-purity charge state exhibits higher brightness and contrast.

We implement real-time control by linking our timing electronics, which consist of an arbitrary-waveform generator (AWG; AWG520 Tektronix) and data-acquisition system (National Instruments, PCIe-6323), with the fast digital logic of a field-programmable gate array (FPGA; Virtex-7 Xilinx); see Fig. 1(a) for the full system overview. In the initialization control loop, the AWG outputs a sequence consisting of a green pump and a red charge probe in a repeating loop; when the FPGA detects that a preset photon-detection threshold has been reached during the charge probe, it sends an event signal to advance the AWG out of its loop and continue with the other predefined measurements. The time it takes from detection of the final photon to the halting of the initialization procedure is $\tau_{\text{delay}} = 550$ ns, which consists of the detector delay (30 ns), the AWG delay (500 ns), and the red-laser delay (20 ns).

III. RESULTS

A. Real-time charge initialization

We characterize the charge-probe process using a photon-distribution model accounting for transitions between N-V^- and the neutral (N-V^0) charge state [28,32,33]. The model assumes that the charge dynamics of the N-V center can be reduced to a two-state system with emission rates γ_- and γ_0, and charge transition rates for ionization (negative to neutral, Γ_{ion}) and recombination (neutral to negative, Γ_{rec}); see Fig. 2(a). We determine these rates as a function of laser power by measuring the photon distributions during an exposure that allows about one ionization event to occur and fitting the data using the model [31]. Since the charge-readout powers used in this work are below the saturation regime, the emission rates scale linearly with laser power, while the ionization and recombination rates scale quadratically with power [18,19].

The control parameters governing the charge-probe process are the laser power (P_{probe}), the maximum duration (τ_{probe}), and the photon threshold (ν) that defines the termination condition of the initialization loop [Fig. 2(a)]. Given these three parameters, the model provides the expected photon distributions for the negative-charge-state and neutral-charge-state configurations,

$$p(n|s), \tag{1}$$

where n is the number of photons detected during τ_{probe} and $s = -$ or 0 signifies the initial charge state; see Fig. 2(b) for an example.

The distributions allow us to calculate two critical metrics for RTI: the N-V^- charge fidelity ($F_{\text{N-}V^-}$) and the average number of attempts ($\bar{n}$) required for successful initialization. The initialization fidelity is governed by two terms,

$$F_{\text{N-}V^-} = (1-\epsilon_T)(1-\epsilon_D), \tag{2}$$

where ϵ_T is the threshold error and ϵ_D is the delay error. The threshold error is the probability that N-V^0 leads to a threshold-reaching event and is given by

$$\epsilon_T = \frac{\sum_{n\geq\nu}(1-P_-)p(n|0)}{\sum_{n\geq\nu}[P_-p(n|-)+(1-P_-)p(n|0)]}, \tag{3}$$

where P_- is the probability that the N-V center was initially in N-V^- before the charge probe. The delay error is the probability that an ionization event occurred during the

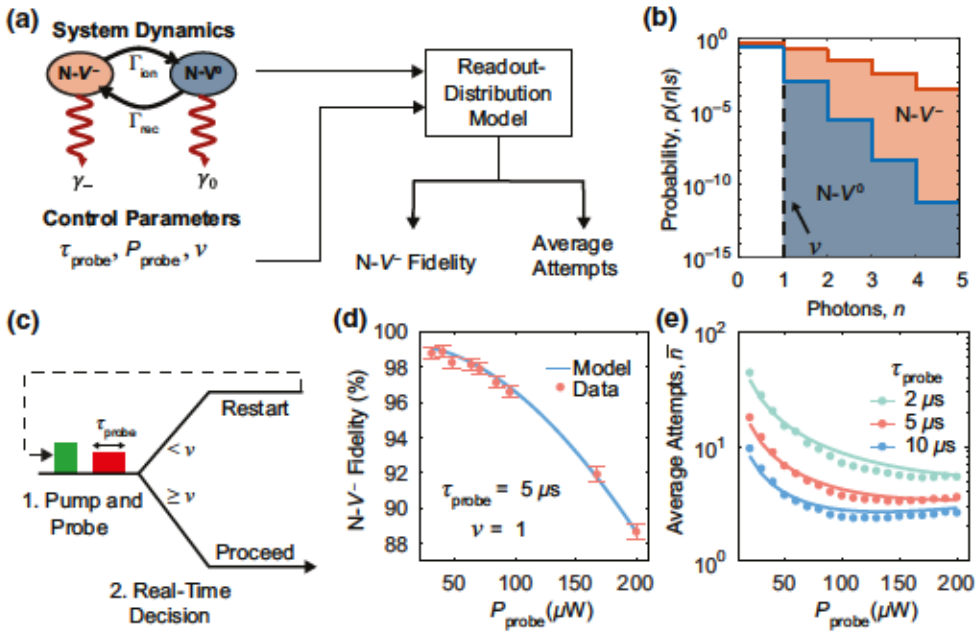

FIG. 2. Modeling real-time control. (a) Conceptual diagram of the model. The system-dynamics model describes how the charge-dependent emission rates (γ_-, γ_0) and charge interconversion rates (Γ_{ion}, Γ_{rec}) depend on illumination power (P_{probe}). Given a readout duration (τ_{probe}) and a threshold condition ($\nu_{\text{threshold}}$), the readout distribution model determines the N-V^- fidelity and the average number of attempts required to reach the threshold. (b) Modeled photon distributions for the two charge states with $\tau_{\text{probe}} = 5\ \mu$s and $P_{\text{probe}} = 100\ \mu$W. (c) Experimental timing diagram and decision tree for initializing the charge state. (d) Comparison between the modeled (line) and measured (markers) N-V^- fidelity as a function of probe power. (e) Comparison between the modeled (lines) and measured (markers) average attempts to reach the threshold ($\nu = 1$) as a function of power and probe duration. Error bars in (e) are comparable to the marker size.

electronic delay time while the laser remains on following a threshold-reaching event and is given by

$$\epsilon_D = 1 - e^{-\tau_{\text{delay}}\Gamma_{\text{ion}}}. \tag{4}$$

The average number of attempts for initialization is given by

$$\bar{n} = \left(\sum_{n\geq\nu} P_{-}p(n|-) + (1-P_{-})p(n|0)\right)^{-1}. \tag{5}$$

As an ensemble average, $\bar{n}$ takes continuous values.

Figure 2(c) outlines the experimental decision tree in the real-time initialization procedure. A charge pump-and-probe sequence is repeatedly played out by the AWG until the FPGA detects a threshold-reaching event. The green pump pulse is set to 500 μW and 500 ns to quickly repump the charge without incurring significant overhead; we vary P_{probe} and τ_{probe} to optimize the performance. To verify our model, we measure $F_{\text{N-}V^-}$ and $\bar{n}$ as a function of P_{probe} as shown in Figs. 2(d) and 2(e). We extract $F_{\text{N-}V^-}$ by performing a subsequent charge measurement and fitting to the photon-distribution model, and we determine $\bar{n}$ from the time it takes to record 10^5 threshold-reaching events.

The measurements of $F_{\text{N-}V^-}$ are generally consistent with our model. We attribute the small discrepancy between the measured values of $\bar{n}$ and the model predictions to minor variations in the steady-state charge population imposed by the control sequence. The model assumes a fixed initial N-V^- population of $P_- = 75\%$; however, we observe that the initial population depends weakly on the probe duration and power used in a repeated experiment. We ignore this higher-order effect since it has the beneficial effect of decreasing $\bar{n}$ for the control parameters we use.

The relative contributions of the two error sources in the charge initialization fidelity depend on P_{probe}; see Fig. 3. At low powers, ϵ_T is dominant and $F_{\text{N-}V^-}$ is limited by the signal-to-background ratio of the charge-readout process. For a threshold of one photon, the maximum achievable fidelity is $(98.6 \pm 0.2)\%$ as P_{probe} approaches zero, however $\bar{n}$ becomes large; see Fig. 2(e). At higher powers, ϵ_D is dominant due to the quadratic scaling of the ionization rate with power. Therefore, when designing an experiment using RTI that is sensitive to timing overheads, it is crucial to minimize the control delay time to maintain high initial fidelity along with a small $\bar{n}$.

To verify that RTI preserves the ground-state spin properties, we measure the coherence times for Ramsey (T_2^*) and Hahn-echo (T_2) sequences, as well as the spin relaxation time (T_1) [31]. We observe an approximately 16% increase in T_2^* when using RTI, which could be due to ionization of nearby neutrally charged substitutional nitrogen donors ($S = 1/2$) to the positive charge state ($S = 0$) [34]. We detect no statistically significant difference in T_2 or T_1.

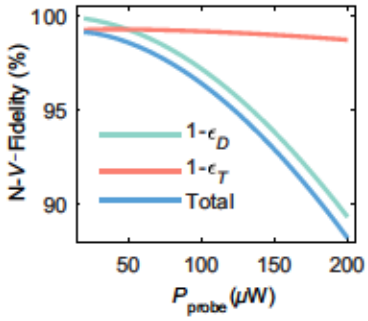

FIG. 3. Initialization errors. Modeled $F_{\text{N-}V^-}$ as a function of P_{probe} together with the independent contributions due to thresholding and delay errors. The model parameters are the same as in Fig. 2(d).

B. Spin-readout performance

We now consider the effect of the initial $F_{\text{N-}V^-}$ on the spin-readout SNR. Generally, the observable for a spin measurement of a N-V center follows the form

$$\langle S_i \rangle = \langle \tilde{S}_i \rangle F_{\text{N-}V^-} + \langle \epsilon \rangle (1 - F_{\text{N-}V^-}), \tag{6}$$

where $\langle S_i \rangle$ is ensemble-averaged value of the observable S for the spin state i, $\langle \tilde{S}_i \rangle$ is the expectation value of the observable for spin state i given an initial N-V^- state, and $\langle \epsilon \rangle$ is an error in the observable that is due to the N-V center residing in N-V^0 during the readout. The single-shot SNR for spin readout is then given by

$$\mathcal{R} = \frac{|\langle S_0 \rangle - \langle S_1 \rangle|}{\sqrt{\sigma_0^2 + \sigma_1^2}}, \tag{7}$$

where σ_i is the standard deviation associated with $\langle S_i \rangle$ [7].

To make quantitative comparisons between readout techniques, the physical observable and its accompanying statistical model must be incorporated into Eq. (7). For PL readout [Fig. 4(a)], the signal is the average number of detected photons during the first 250 ns of 532-nm illumination and thus obeys Poissonian statistics. For SCC readout [Fig. 4(b)], the signal is the probability of detecting N-V^- following the conversion, and it obeys binomial statistics.

Figure 4(c) shows the measurement timing diagram that allows the characterization of spin SNR as a function of $F_{\text{N-}V^-}$. Following initialization with an arbitrary $F_{\text{N-}V^-}$, the spin state is either left in the polarized $m_s = 0$ state or flipped to the $m_s = -1$ state with a 40-ns microwave π pulse. We estimate the value of $\langle S_i \rangle$ from repeated measurements using both traditional-readout and SCC-readout techniques. We also measure the spin SNR for the traditional SSI consisting of 2 μs of 532-nm illumination. We separately optimize the PL-readout and SCC-readout parameters to ensure a fair comparison between the techniques [31]. The raw data are fit with Eq. (6), from which

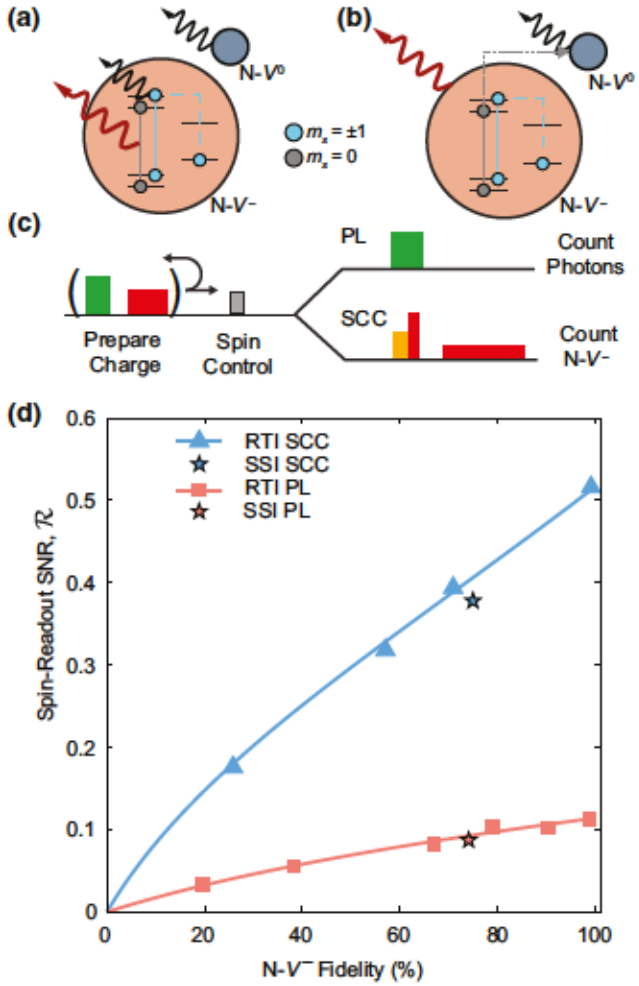

FIG. 4. Spin-readout performance. (a),(b) Conceptual diagrams for traditional PL readout (a) and SCC readout (b). Red curves represent the desired signal and black curves contribute to background. (c) Timing diagram for measuring the spin SNR given different heralded charge fidelity. (d) Spin-readout SNR as a function of N-V^- fidelity for different initialization and readout techniques. The solid lines represent a fit of Eq. (6) to the data, where the fit and data are converted to SNR with use of Eq. (7). Error bars are comparable in size to the markers.

we empirically determine $\langle \tilde{S}_I \rangle$ and $\langle \epsilon \rangle$. Figure 4(d) depicts the results of this measurement for both readout protocols, with the SNR calculated with Eq. (7) for both the data (symbols) and the fits (curves).

The spin SNR following RTI for both SCC readout and PL readout, when N-V^- fidelity is controlled for, is approximately 7% higher than for SSI. This is attributed to improved optical spin polarization in the real-time protocol, since the red laser induces negligible recombination; this is consistent with previous observations [35]. The initial spin purity, estimated from measurements of the excited-state lifetime, is approximately 91% for the steady-state protocol and approximately 94% for the real-time protocol [31,36,37].

C. Spin-readout efficiency

By combining the RTI model with the spin SNR as a function of $F_{\text{N-}V^-}$, we can optimize the signal acquisition for a given experiment. To achieve this, we define the spin-readout efficiency,

$$\xi = \frac{\mathcal{R}}{\sqrt{\tau_I + \tau_O + \tau_R}}, \tag{8}$$

where τ_I is the initialization time, τ_O is the spin operation time, and τ_R is the spin-readout time. This figure of merit is related to the sensitivity, and encompasses the single-shot SNR, the spin operation duration, and the associated initialization and readout overheads [7]. The total SNR after multiple measurement cycles with total integration time T is given simply by $\langle \mathcal{R} \rangle = \xi \sqrt{T}$. We assume the operation time is fixed by the desired sensing or computation protocol. We previously considered the optimization of the readout duration, power, and threshold for SCC, and we include those procedures when necessary [7,38].

Real-time control allows additional design flexibility in an experiment, as longer time spent initializing results in a higher spin-readout SNR yet fewer total averages. Equation (8) quantitatively captures the trade-off between these two quantities. The initialization time is given by

$$\tau_I = (\tau_{\text{pump}} + \tau_{\text{overhead}} + \tau_{\text{probe}})\bar{n}, \tag{9}$$

where $\tau_{\text{pump}} = 0.5\ \mu$s is the duration of the 532-nm charge-reset pump and $\tau_{\text{overhead}} = 1.5\ \mu$s is the overhead in the initialization sequence comprising the green AOM delay, singlet decay time, and τ_{delay}. Note that τ_I is an average quantity since Eq. (8) is assumed to be an ensemble average over many trials.

With a model describing the readout efficiency, we can numerically optimize Eq. (8) to determine the protocol parameters that maximize the readout efficiency for a given operation time. To assess the results in context of typical N-V-center experiments, we compute and measure the baseline readout efficiency, ξ_{baseline}, corresponding to steady-state initialization and traditional PL readout for different operation times. We then define the speedup as the reduction in integration time required to achieve a fixed SNR when comparing a new technique with the baseline,

$$\Xi = \left(\frac{\xi}{\xi_{\text{baseline}}}\right)^2. \tag{10}$$

A speedup of unity defines the break-even time, τ_{BE}, the operation time at which it is equally efficient to use the enhanced technique over the baseline protocol.

Figure 5 presents the results of this optimization for four different scenarios: SSI with PL readout, RTI with PL readout, SSI with SCC readout, and RTI with SCC readout. The predicted and measured speedup curves for

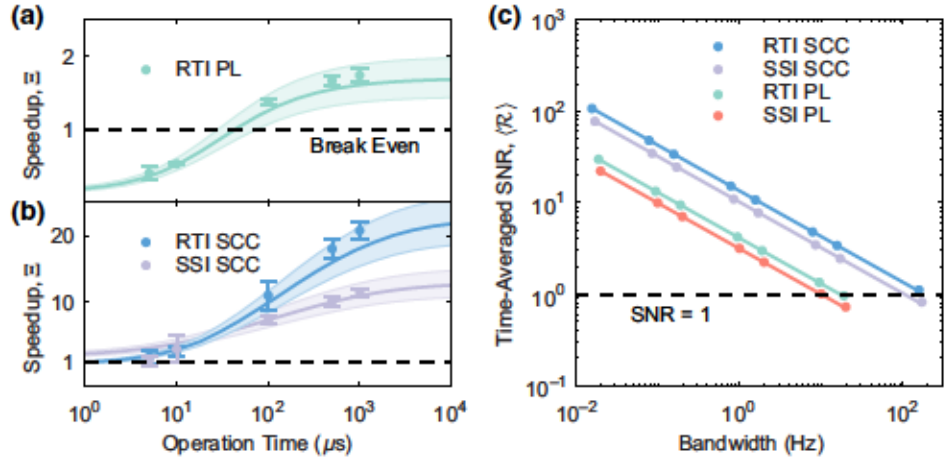

FIG. 5. Performance improvements for time-averaged measurements. Predicted (curves) and measured (data points) speedup for PL spin readout with RTI (a) and SCC readout using SSI and RTI (b). The dashed black line in (a),(b) indicates the break-even condition in comparison with SSI and PL readout. The shaded regions represent 1σ confidence intervals of the model, accounting for uncertainty in the measured single-shot SNR. (c) Total time-averaged SNR as a function of integration bandwidth for each protocol. Lines are fits to the inverse square root of the bandwidth. Error bars in (c) are smaller than the markers.

PL and SCC readout are shown in Figs. 5(a) and 5(b), respectively. For PL readout, we observe a break-even time for using RTI of $\tau_{\mathrm{BE}} \sim 70\ \mu$s, and a maximum speedup of 1.74 ± 0.09 for an operation time of 1 ms. We find that our full model always results in a choice of measurement parameters that make SCC readout more efficient than PL readout. RTI offers a further boost for operation times of more than 30 μs, with a maximum observed speedup of 20.8 ± 1.2 for $\tau_O = 1$ ms. The measurements agree with the model prediction when the uncertainty in calibrating the single-shot SNR is accounted for.

Figure 5(c) shows the total SNR as a function of integration bandwidths for each of the four techniques. Here we have fixed the operation time to be 500 μs. In each case, the total SNR scales with the inverse square root of the bandwidth as expected. Of note is the integration bandwidth for which each technique achieves $\langle \mathcal{R} \rangle = 1$, which represents the maximum frequency of environmental dynamics that can be resolved above the noise. The RTI protocol coupled with SCC readout offers the best performance for this operation time. In addition, Fig. 5(c) confirms that the optical pulse sequences required for RTI and SCC readout do not introduce any appreciable noise in the bandwidth we consider.

IV. DISCUSSION

A. Sensitivity improvements

N-V-center quantum sensors stand to gain significant sensitivity improvements from the use of RTI protocols. The largest speedup is realized for long operation times that approach 1 ms, which coincide with the typical requirements for spin relaxometry [14,39] as well as dynamical decoupling sequences [40,41].

The single N-V center studied here exhibits a Hahn-echo $T_2 \approx 800\ \mu$s [31]. We estimate the ac magnetic field sensitivity for our N-V center using the expression

$$\eta_{\mathrm{ac}} = \frac{\pi\hbar}{2g\mu_B}\sqrt{\frac{T_2 + \tau_I + \tau_R}{T_2^2}}\sigma_R, \tag{11}$$

where g is the gyromagnetic ratio, μ_B is the Bohr magneton, and σ_R is the spin-readout noise [28]. The spin-readout noise is directly related to the single-shot SNR through the following expression [7]:

$$\sigma_R = \sqrt{1 + \frac{2}{\mathcal{R}^2}}. \tag{12}$$

Our optimization routine for $\tau_O = T_2 = 800\ \mu$s yields the following parameters for RTI and SCC readout: $\tau_I = 43\ \mu$s, $P_{\mathrm{init}} = 53\ \mu$W, $\tau_R = 127\ \mu$s, and $P_{\mathrm{readout}} = 22\ \mu$W. With these parameters, the predicted $\mathcal{R} = 0.4$ corresponds to $\sigma_R = 3.67$ and $\eta_{\mathrm{ac}} = 1.3\ \mathrm{nT/Hz^{1/2}}$. The optimal parameters from the model correspond to a charge initialization fidelity of $F_{\mathrm{N\text{-}}V^-} = 98.6\%$ and a charge-readout fidelity of 70%. The charge-readout fidelity is significantly below the achievable maximum of approximately 95%. This implies that, for this operation time, it is advantageous to perform additional averaging of less-accurate measurements.

We have emphasized the use of RTI together with SCC readout, since the two methods have similar experimental requirements. However, the benefits extend to other N-V-center readout techniques used in quantum sensors, such

as the nuclear-assisted method [10,42], which would see similar signal-acquisition improvements due to RTI of the charge state.

B. Gains for N-V centers near surfaces

In many situations, the gains from RTI are likely to be even larger than we have demonstrated, since N-V centers located in nanodiamonds or close to surfaces typically exhibit lower steady-state charge populations than those in bulk diamond [20,38]. With use of our model and the assumption of a 25% N-V^- steady-state population, RTI would enable a factor-of-6 speedup for PL readout and a factor-of-75 speedup for SCC readout with an operation time of 500 μs.

C. Role of photon-collection efficiency

For any quantum device based on PL detection, the performance depends critically on the photon-collection efficiency [7]. The need to maximize photon count rates forces trade-offs in device design, optical complexity, and versatility of N-V centers in different applications. Figure 6 shows the predicted speedup and corresponding break-even times for the use of charge-state RTI across a range of values for the saturated PL count rate from a single N-V center corresponding to typical experimental situations. The predictions in Fig. 6 are calculated by scaling the parameters in our model that depend on photon-collection efficiency, corresponding to our measured saturated count rate under 532-nm illumination of 300 000 counts/s [31]. Of note are the experimentally relevant saturated count rates of 60 000, 125 000, 600 000, and 900 000 counts/s. Respectively, these values approximate a N-V center imaged through a planar diamond surface with a high-NA air objective, a planar sample using an oil-immersion objective [43], a ⟨111⟩-oriented diamond with a solid immersion lens and an air objective [44], and a diamond nanobeam [28]. These values are marked as points in Fig. 6.

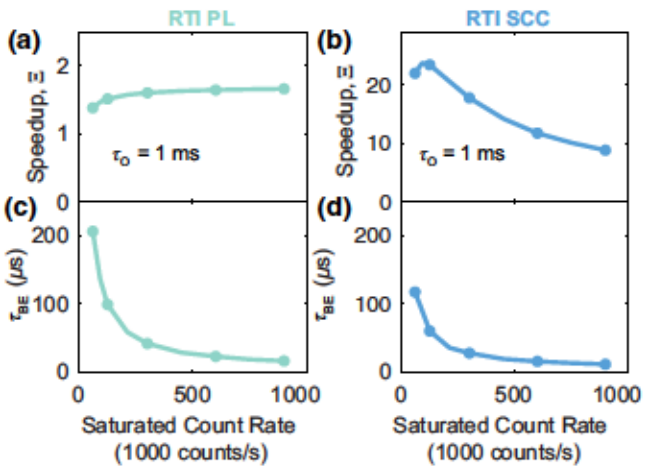

FIG. 6. The effect of photon-collection efficiency. (a),(b) Predicted speedup for $\tau_O = 1$ ms obtained with RTI together with PL readout (a) or SSC readout (b) as a function of saturated photon count rate under 532-nm illumination. (c),(d) Predicted break-even time, at which it becomes advantageous to use RTI, for the same parameters as in (a),(b). Points represent the experimentally relevant count rates mentioned in the text.

Notably, the speedup from RTI persists across this range of relevant photon-collection efficiencies. The speedups in Figs. 6(a) and 6(b) are calculated according to Eq. (10) in comparison with a baseline of SSI and PL readout predicted for the corresponding experimental situation with $\tau_O = 1$ ms. The speedup for PL readout is essentially independent of the collection efficiency; for SCC readout the gains are largest for systems with low collection efficiency, where the relative improvement of using SCC readout over PL readout is magnified. The combined approach of RTI and SCC readout still yields nearly an-order-of-magnitude speedup even for count rates approaching 1×10^6 counts/s.

The break-even times shown in Figs. 6(c) and 6(d) correspond to the value of τ_O for which the spin-readout efficiency obtained with RTI equals that for SSI, using the corresponding readout protocol. Increasing collection efficiency results in increased charge initialization fidelity, and a corresponding reduction in τ_{BE}. For high-collection-efficiency devices with saturated count rates approaching 1×10^6 counts/s, the break-even time for using RTI is reduced to 16 μs for PL readout and 11 μs for SCC readout.

D. Maximizing the initial state fidelity

While we have focused on applications that require consideration of the overhead from initialization and readout, the RTI technique can be readily adapted to situations in which initialization fidelity is prioritized over total measurement time. For example, the initialization error can be reduced by a factor of 2 by increasing the threshold to two photons and decreasing P_{probe}. Using $\nu = 2$ and $\tau_I = 7$ ms in our setup, we measure $F_{\text{N-}V^-} = (99.4 \pm 0.1)\%$ [31]. Such control over the charge state could facilitate precise measurements of the local electrostatic environment [20,45], aid in the quantification of photon-collection efficiency for photonic devices [46], and increase the single-shot SNR for infrequent SCC measurements [47]. In addition, the fidelity associated with initializing, controlling, and measuring coupled nuclear spins [17,21,30] is intricately tied to the N-V center's charge and spin purity and thus could be increased with RTI.

V. CONCLUSION

We demonstrate an efficient method for initializing the charge state of a N-V center in real time and assess how this

can be used to increase the efficiency of spin readout. Real-time control could be applied to other aspects of the N-V center, such as projective initialization of nuclear spins [48] and increasing the spin-state initialization fidelity through time gating. In addition, this advanced control can be applied to other emerging solid-state spin defects, especially those that have a high-fidelity-readout mechanism but a less-than-ideal spin or charge pumping transition.

ACKNOWLEDGMENTS

This work was supported by the National Science Foundation under Grants No. ECCS-1553511 (D.A.H., J.D.L., and L.C.B.) and No. ECCS-1842655 (T.-Y.H. and L.C.B.). The authors thank H.S. Knowles and Z. Zhang for useful discussions and D. Bluvstein, S.A. Breitweiser, and R.N. Patel for valuable comments on the manuscript.

D.A. Hopper and J.D. Lauigan contributed equally to this work.

[1] C. L. Degen, F. Reinhard, and P. Cappellaro, Quantum sensing, Rev. Mod. Phys. **89**, 35002 (2017).

[2] S. Wehner, D. Elkouss, and R. Hanson, Quantum internet: A vision for the road ahead, Science **362**, eaam9288 (2018).

[3] D. D. Awschalom, R. Hanson, J. Wrachtrup, and B. B. Zhou, Quantum technologies with optically interfaced solid-state spins, Nat. Photonics **12**, 516 (2018).

[4] T. Schröder, S. L. Mouradian, J. Zheng, M. E. Trusheim, M. Walsh, E. H. Chen, L. Li, I. Bayn, and D. Englund, Quantum nanophotonics in diamond, J. Opt. Soc. Am. B **33**, B65 (2016).

[5] M. Atatüre, D. Englund, N. Vamivakas, S.-Y. Lee, and J. Wrachtrup, Material platforms for spin-based photonic quantum technologies, Nat. Rev. Mater. **3**, 38 (2018).

[6] M. W. Doherty, N. B. Manson, P. Delaney, F. Jelezko, J. Wrachtrup, and L. C. Hollenberg, The nitrogen-vacancy colour centre in diamond, Phys. Rep. **528**, 1 (2013).

[7] D. A. Hopper, H. J. Shulevitz, and L. C. Bassett, Spin readout techniques of the nitrogen-vacancy center in diamond, Micromachines **9**, 437 (2018).

[8] J. F. Barry, M. J. Turner, J. M. Schloss, D. R. Glenn, Y. Song, M. D. Lukin, H. Park, and R. L. Walsworth, Optical magnetic detection of single-neuron action potentials using quantum defects in diamond, Proc. Natl. Acad. Sci. U.S.A. **113**, 14133 (2016).

[9] I. Lovchinsky, J. D. Sanchez-Yamagishi, E. K. Urbach, S. Choi, S. Fang, T. I. Andersen, K. Watanabe, T. Taniguchi, A. Bylinskii, E. Kaxiras, P. Kim, H. Park, and M. D. Lukin, Magnetic resonance spectroscopy of an atomically thin material using a single-spin qubit, Science **355**, 503 (2017).

[10] N. Aslam, M. Pfender, P. Neumann, R. Reuter, A. Zappe, F. Fávaro de Oliveira, A. Denisenko, H. Sumiya, S. Onoda, J. Isoya, and J. Wrachtrup, Nanoscale nuclear magnetic resonance with chemical resolution, Science **357**, 67 (2017).

[11] J. M. Boss, K. S. Cujia, J. Zopes, and C. L. Degen, Quantum sensing with arbitrary frequency resolution, Science **356**, 837 (2017).

[12] S. Schmitt, T. Gefen, F. M. Stürner, T. Unden, G. Wolff, C. Müller, J. Scheuer, B. Naydenov, M. Markham, S. Pezzagna, J. Meijer, I. Schwarz, M. Plenio, A. Retzker, L. P. McGuinness, and F. Jelezko, Submillihertz magnetic spectroscopy performed with a nanoscale quantum sensor, Science **356**, 832 (2017).

[13] I. Gross, W. Akhtar, V. Garcia, L. J. Martínez, S. Chouaieb, K. Garcia, C. Carrétéro, A. Barthélémy, P. Appel, P. Maletinsky, J.-V. Kim, J. Y. Chauleau, N. Jaouen, M. Viret, M. Bibes, S. Fusil, and V. Jacques, Real-space imaging of non-collinear antiferromagnetic order with a single-spin magnetometer, Nature **549**, 252 (2017).

[14] A. Ariyaratne, D. Bluvstein, B. A. Myers, and A. C. B. Jayich, Nanoscale electrical conductivity imaging using a nitrogen-vacancy center in diamond, Nat. Commun. **9**, 2406 (2018).

[15] B. Hensen, H. Bernien, A. E. Dréau, A. Reiserer, N. Kalb, M. S. Blok, J. Ruitenberg, R. F. L. Vermeulen, R. N. Schouten, C. Abellán, W. Amaya, V. Pruneri, M. W. Mitchell, M. Markham, D. J. Twitchen, D. Elkouss, S. Wehner, T. H. Taminiau, and R. Hanson, Loophole-free Bell inequality violation using electron spins separated by 1.3 kilometres, Nature **526**, 682 (2015).

[16] P. C. Humphreys, N. Kalb, J. P. J. Morits, R. N. Schouten, R. F. L. Vermeulen, D. J. Twitchen, M. Markham, and R. Hanson, Deterministic delivery of remote entanglement on a quantum network, Nature **558**, 268 (2018).

[17] C. E. Bradley, J. Randall, M. H. Abobeih, R. C. Berrevoets, M. J. Degen, M. A. Bakker, M. Markham, D. J. Twitchen, and T. H. Taminiau, A Ten-Qubit Solid-State Spin Register with Quantum Memory up to One Minute, Phys. Rev. X **9**, 031045 (2019).

[18] G. Waldherr, J. Beck, M. Steiner, P. Neumann, A. Gali, T. Frauenheim, F. Jelezko, and J. Wrachtrup, Dark States of Single Nitrogen-Vacancy Centers in Diamond Unraveled by Single Shot NMR, Phys. Rev. Lett. **106**, 157601 (2011).

[19] N. Aslam, G. Waldherr, P. Neumann, F. Jelezko, and J. Wrachtrup, Photo-induced ionization dynamics of the nitrogen vacancy defect in diamond investigated by single-shot charge state detection, New J. Phys. **15**, 13064 (2013).

[20] D. Bluvstein, Z. Zhang, and A. C. B. Jayich, Identifying and Mitigating Charge Instabilities in Shallow Diamond Nitrogen-Vacancy Centers, Phys. Rev. Lett. **122**, 76101 (2019).

[21] P. Neumann, J. Beck, M. Steiner, F. Rempp, H. Fedder, P. R. Hemmer, J. Wrachtrup, and F. Jelezko, single-shot readout of a Single nuclear spin, Science **329**, 542 (2010).

[22] Y. Doi, T. Makino, H. Kato, D. Takeuchi, M. Ogura, H. Okushi, H. Morishita, T. Tashima, S. Miwa, S. Yamasaki, P. Neumann, J. Wrachtrup, Y. Suzuki, and N. Mizuochi, Deterministic Electrical Charge-State Initialization of Single Nitrogen-Vacancy Center in Diamond, Phys. Rev. X **4**, 11057 (2014).

[23] Y. Doi, T. Fukui, H. Kato, T. Makino, S. Yamasaki, T. Tashima, H. Morishita, S. Miwa, F. Jelezko, Y. Suzuki, and N. Mizuochi, Pure negatively charged state of the NV center in n-type diamond, Phys. Rev. B **93**, 81203(R) (2016).

[24] D. A. Hopper, R. R. Grote, A. L. Exarhos, and L. C. Bassett, Near-infrared-assisted charge control and spin readout of

the nitrogen-vacancy center in diamond, Phys. Rev. B **94**, 241201(R) (2016).

[25] G. Waldherr, P. Neumann, S. F. Huelga, F. Jelezko, and J. Wrachtrup, Violation of a Temporal Bell Inequality for Single Spins in a Diamond Defect Center, Phys. Rev. Lett. **107**, 090401 (2011).

[26] G. Waldherr, J. Beck, P. Neumann, R. S. Said, M. Nitsche, M. L. Markham, D. J. Twitchen, J. Twamley, F. Jelezko, and J. Wrachtrup, High-dynamic-range magnetometry with a single nuclear spin in diamond, Nat. Nanotechnol. **7**, 105 (2012).

[27] G. Waldherr, Y. Wang, S. Zaiser, M. Jamali, T. Schulte-Herbruggen, H. Abe, T. Ohshima, J. Isoya, J. F. Du, P. Neumann, and J. Wrachtrup, Quantum error correction in a solid-state hybrid spin register, Nature **506**, 204 (2014).

[28] B. J. Shields, Q. P. Unterreithmeier, N. P. de Leon, H. Park, and M. D. Lukin, Efficient Readout of a Single Spin State in Diamond via Spin-to-Charge Conversion, Phys. Rev. Lett. **114**, 136402 (2015).

[29] H. Bernien, B. Hensen, W. Pfaff, G. Koolstra, M. S. Blok, L. Robledo, T. H. Taminiau, M. Markham, D. J. Twitchen, L. Childress, and R. Hanson, Heralded entanglement between solid-state qubits separated by three metres, Nature **497**, 86 (2013).

[30] J. Cramer, N. Kalb, M. A. Rol, B. Hensen, M. S. Blok, M. Markham, D. J. Twitchen, R. Hanson, and T. H. Taminiau, Repeated quantum error correction on a continuously encoded qubit by real-time feedback, Nat. Commun. **7**, 11526 (2016).

[31] See Supplemental Material at http://link.aps.org/supplemental/10.1103/PhysRevApplied.13.024016 for details on the setup, spin-readout calibrations, collection-efficiency calculations, and charge-readout method.

[32] B. D'Anjou, L. Kuret, L. Childress, and W. A. Coish, Maximal Adaptive-Decision Speedups in Quantum-State Readout, Phys. Rev. X **6**, 011017 (2016).

[33] L. Hacquebard and L. Childress, Charge-state dynamics during excitation and depletion of the nitrogen-vacancy center in diamond, Phys. Rev. A **97**, 63408 (2018).

[34] M. W. Doherty, C. A. Meriles, A. Alkauskas, H. Fedder, M. J. Sellars, and N. B. Manson, Towards a Room-Temperature Spin Quantum Bus in Diamond via Electron Photoionization, Transport, and Capture, Phys. Rev. X **6**, 041035 (2016).

[35] X.-D. Chen, L.-M. Zhou, C.-L. Zou, C.-C. Li, Y. Dong, F.-W. Sun, and G.-C. Guo, Spin depolarization effect induced by charge state conversion of nitrogen vacancy center in diamond, Phys. Rev. B **92**, 104301 (2015).

[36] G. D. Fuchs, V. V. Dobrovitski, D. M. Toyli, F. J. Heremans, C. D. Weis, T. Schenkel, and D. D. Awschalom, Excited-state spin coherence of a single nitrogen-vacancy centre in diamond, Nat. Phys. **6**, 668 (2010).

[37] L. Robledo, H. Bernien, T. V. D. Sar, R. Hanson, T. van der Sar, and R. Hanson, Spin dynamics in the optical cycle of single nitrogen-vacancy centres in diamond, New J. Phys. **13**, 25013 (2011).

[38] D. A. Hopper, R. R. Grote, S. M. Parks, and L. C. Bassett, Amplified sensitivity of nitrogen-vacancy spins in nanodiamonds using all-optical charge readout, ACS Nano **12**, 4678 (2018).

[39] M. Pelliccione, B. A. Myers, L. M. A. Pascal, A. Das, and A. C. Bleszynski Jayich, Two-Dimensional Nanoscale Imaging of Gadolinium Spins via Scanning Probe Relaxometry with a Single Spin in Diamond, Phys. Rev. Appl. **2**, 054014 (2014).

[40] T. H. Taminiau, J. J. T. Wagenaar, T. van der Sar, F. Jelezko, V. V. Dobrovitski, and R. Hanson, Detection and Control of Individual Nuclear Spins Using a Weakly Coupled Electron Spin, Phys. Rev. Lett. **109**, 137602 (2012).

[41] S. Kolkowitz, Q. P. Unterreithmeier, S. D. Bennett, and M. D. Lukin, Sensing Distant Nuclear Spins with a Single Electron Spin, Phys. Rev. Lett. **109**, 137601 (2012).

[42] T. Häberle, T. Oeckinghaus, D. Schmid-Lorch, M. Pfender, F. F. de Oliveira, S. A. Momenzadeh, A. Finkler, and J. Wrachtrup, Nuclear quantum-assisted magnetometer, Rev. Sci. Instrum. **88**, 13702 (2017).

[43] I. Lovchinsky, A. O. Sushkov, E. Urbach, N. P. de Leon, S. Choi, K. De Greve, R. Evans, R. Gertner, E. Bersin, C. Müller, L. McGuinness, F. Jelezko, R. L. Walsworth, H. Park, and M. D. Lukin, Nuclear magnetic resonance detection and spectroscopy of single proteins using quantum logic, Science **351**, 836 (2016).

[44] M. Jamali, I. Gerhardt, M. Rezai, K. Frenner, H. Fedder, and J. J. Wrachtrup, Microscopic diamond solid-immersion-lenses fabricated around single defect centers by focused ion beam milling, Rev. Sci. Instrum. **85**, 123703 (2014).

[45] T. Mittiga, S. Hsieh, C. Zu, B. Kobrin, F. Machado, P. Bhattacharyya, N. Z. Rui, A. Jarmola, S. Choi, D. Budker, and N. Y. Yao, Imaging the Local Charge Environment of Nitrogen-Vacancy Centers in Diamond, Phys. Rev. Lett. **121**, 246402 (2018).

[46] T.-Y. Huang, R. R. Grote, S. A. Mann, D. A. Hopper, A. L. Exarhos, G. G. Lopez, G. R. Kaighn, E. C. Garnett, and L. C. Bassett, A monolithic immersion metalens for imaging solid-state quantum emitters, Nat. Commun. **10**, 2392 (2019).

[47] J.-C. Jaskula, B. J. Shields, E. Bauch, M. D. Lukin, A. S. Trifonov, and R. L. Walsworth, Improved Quantum Sensing with a Single Solid-State Spin via Spin-to-Charge Conversion, Phys. Rev. Appl. **11**, 64003 (2019).

[48] G.-Q. Liu, J. Xing, W.-L. Ma, P. Wang, C.-H. Li, H. C. Po, Y.-R. Zhang, H. Fan, R.-B. Liu, and X.-Y. Pan, Single-Shot Readout of a Nuclear Spin Weakly Coupled to a Nitrogen-Vacancy Center at Room Temperature, Phys. Rev. Lett. **118**, 150504 (2017).